Chapter 2
Core–Shell Magnetic Nanoclusters

Jinlan Wang and X.C. Zeng

Abstract Nanoclusters, aggregates of a few tens to millions of atoms or molecules, have been extensively studied over the past decades. Core–shell nanoclusters have received increasing attention because of their tunable physical and chemical properties through controlling chemical composition and relative sizes of core and shell. The magnetic core–shell nanoclusters are of particular interests because these heterogeneous nanostructures offer opportunities for developing devices and cluster-assembled materials with new functions for magnetic recording, bio, and medical applications.

The purpose of this review is to report latest progress in the experimental and theoretical studies of bimetallic magnetic core–shell nanoclusters (e.g., at least one component of the constitution is magnetic). Due to page limit, a concise survey of synthetic techniques and main experimental characterizations for magnetic properties is presented. A more detailed overview is given to previous theoretical work.

2.1 Introduction

Nanolusters (or nanoparticles), aggregates of a few tens to millions of atoms or molecules, have attracted enormous interest from either basic science or application point of view in the past decades. From basic science point of view, nanoclusters are species intermediate in size between microscopic atoms or molecules and macroscopic bulk matter, and these may be considered as new forms of matter or superatoms that display properties very different from their molecular and bulk counterparts. Small nanoclusters can show strongly size-dependent characteristics, for example, their structures can vary dramatically with size. Among others, manifestation of this strong-size dependence includes behavior of "magic number" clusters,

X.C. Zeng (✉)
Department of Chemistry and Nebraska Center for Materials and Nanoscience, University of Nebraska, Lincoln, Nebraska 68588, USA
e-mail: xzengl@unl.edu

J.P. Liu et al. (eds.), *Nanoscale Magnetic Materials and Applications*,
DOI 10.1007/978-0-387-85600-1_2,

metal–nonmetal transition, nonmagnetic–magnetic transition, red or blue shift of optical gap, and selective catalysis [1, 11, 12, 24, 31, 42, 60]. The intriguing properties of nanoclusters stem from their finite size, large surface-to-volume ratio, and quantum effect. From application point of view, highly stable nanoclusters can serve as building blocks for assembly of new materials and for design of nano-devices. Size-dependent characteristics also open a possibility for tailoring properties of nanoclusters by precisely controlling the formation process.

Nanoclusters are usually produced from mass-selective cluster beams and can be studied in the gas phase, or within an inert matrix, or adsorbed onto a surface. Many technologies such as mass spectrometry; ion mobility spectrometry; photo- and collision-induced dissociation; photoionization, photoelectron, and infrared spectroscopies; electron paramagnetic resonance; Stern–Galach molecular-beam deflection; and optical spectroscopy have been advanced to measure the energy, ionization potential, electron affinity, magnetic moment, and optical absorption of nanoclusters.

Theoretical computations have also played a key role in the cluster science since certain properties of nanoclusters are difficult to measure, and many conventional theories developed for treatment of atomic/molecular systems or bulk matter are inapplicable to nanoscale systems. Common computational tools include empirical potential methods such as molecular dynamics and Monte Carlo simulation, semi-empirical methods such as tight-binding approximation, and first-principles methods or ab initio electronic structure calculations such as density functional theory and molecular orbital methods. In particular, the density functional theory has become a de facto tool for the study of nanoclusters with more than a few tens of atoms.

Current investigations in cluster science can be loosely categorized into two main areas. One is to understand how the structures and properties of the matter evolve from isolated atom or molecule to nanoparticle and to the bulk as the size increases. Another is to explore new cluster-assembled materials for practical applications, such as novel electronic and optical devices, chemical sensors, and efficient and selective catalysts.

Core–shell nanoclusters have recently received considerable attention owing to their physical and chemical properties that are strongly dependent on the structure of the core, shell, and interface. This structure dependence opens possibility for tuning properties by controlling their chemical composition and relative size of the core and shell. The core–shell magnetic nanoclusters are of special interests since the heterogeneous nanostructures offer opportunities for developing devices and cluster-assembled materials with new functions for magnetic recording, bio, and medical applications. In fact, superparamagnetic nanoparticles with suitable biocompatible coatings have important implications in biology, biotechnology, and other biomedical disciplines [36, 44, 35].

The purpose of this review is to survey most recent studies on bimetallic magnetic core–shell nanoclusters. Toward this end, we will mainly focus on core–shell nanoclusters with at least one component of the constitution being magnetic. Other fascinating topics – for example, binary clusters and nanoalloys, whose structures

are neither core–shell nor magnetic – are completely left out for space reasons. The metal-oxide core–shell clusters are also not discussed in this chapter, although these species can be magnetic. Readers interested in these topics are referred to [8, 10, 17, 41, 43]. Nevertheless, even on the topics that we are focusing we do not claim to be exhaustive. If some contributions are left out, we apologize in advance. We will review previous experimental and theoretical studies: On the experimental part, we present a brief summary of known synthetic technology and measured magnetic properties. On the theoretical part, we provide more detailed review since much less theoretical work has been published in the literature.

The review is organized as follows. In Section 2.2, we give a short description of the experimental techniques for the fabrication of core–shell nanoclusters, as well as a survey of previous analysis and characterization of clusters' structures, components, size, and magnetic properties. In Section 2.3, we summarize previous theoretical work on the core–shell clusters and discuss their structural, electronic, and magnetic properties with different core and shell. Specifically, magnetic systems including iron-, cobalt-, nickel-, manganese-based core–shell clusters are discussed in detail. In Section 2.4, we conclude by providing an outlook for future research about core–shell nanoclusters.

2.2 Experimental Studies of Core–Shell Magnetic Clusters

In this section, we survey the recent progress in fabrication and characterization of magnetic core–shell nanoclusters. The main focuses are placed on three prototype magnetic core/shell nanoclusters, i.e., iron-, cobalt-, nickel-core-based nanoclusters. A list of previous experimental and theoretical studies on the core/shell magnetic nanoclusters is presented in Table 2.1.

Table 2.1 Summary of the recent experimental and theoretical studies on the core–shell magnetic nanoclusters

Clusters	References
Fe@Au	[2, 48, 15, 13, 14, 63, 64, 40, 16, 20, 7, 62, 57, 45]
Co@Au	[48, 3, 4, 5, 6, 39, 61, 9, 58]
Co@Ag	[50, 29, 56, 26, 32, 51, 25, 27, 65, 57]
Co@Cu	[29, 39, 30, 27, 65]
Co@Pt	[46, 47, 39, 34]
Co@Pd	[3, 4, 5, 6, 39]
Ni@Au	[3, 4, 5, 6, 18]
Ni@Ag	[3, 4, 5, 6, 53, 28, 19, 38, 18]
Ni@Pd	[53]
Pt@Co	[54]
Mn@Au	[58]

2.2.1 Iron-Based (Fe@Au) Core–Shell Nanoclusters

Nanometer-sized magnetic particles of iron show promise for practical applications in catalysis, magnetic recording, magnetic fluids, and biomedical applications. However, pure iron nanoparticles are chemically unstable in the air and easily oxidized, which limits their utility. To protect the particles from oxidation, one way is to coat the particles with another inert layer, namely, making a core–shell structure. The core–shell structure is capable of maintaining favorable magnetic properties of metal iron while preventing the nanoparticles from oxidation. Materials such as metal-oxide (iron oxide), inorganic compound (SiO_2), and noble metal (gold and silver) are commonly used as the coating for iron nanoparticles.

Gold has been one of the popular coating materials owing to its chemical inertness, bio-compatibility, non-toxic, and diverse cluster geometries such as planar sheets, cages, and tubes [49, 33, 59, 37]. Indeed, it has been found that gold-coated nanoparticles are more resistant to oxidation and corrosion, compared to the uncoated particles. The gold coating (shell) tends to distribute more uniformly on the spherical particles than on the acicular ones. More importantly, the gold coating is capable of retaining many favorable magnetic properties (such as coercivity or blocking temperature) of the core. The iron-core gold-shell Fe@Au nanoparticles are of particular importance owing to their potential biodiagnostic applications, such as rapid magnetic separation and concentration of biomaterials.

Paulus et al. [48] has fabricated Fe@Au colloidal particles (stabilized by organic ligands) with average sizes of 2 nm and 5.1 nm. They found that the Fe@Au nanopaticles are superparamagnetic at room temperature with the blocking temperature $\mathbf{T}_B \sim 40\,K$. The magnetic anisotropy of Fe@Au is larger than the bulk, which might be caused by the formation of inhomogeneous Fe/Au alloy.

Lin et al. [40] have developed a unique reverse-micelle method to synthesize gold-coated iron (Fe@Au) nanoparticles as illustrated in Fig. 2.1. The average size of Fe@Au nanoparticles is about 10 nm. These nanoparticles are characterized by a combination of transmission electron microscopy (TEM), energy dispersive spectroscopy (EDS), X-ray diffraction (XRD), ultraviolet-visible spectroscopy (UV/vis), and quantum design superconducting quantum interference device (SQUID) magnetometry. The absence of oxygen and iron oxide, based on the EDS and XRD measurements, confirms a complete coating of the iron core by the gold shell. The authors have also found that a red shift and broadening occurs in the absorption band of the Fe@Au colloid as compared to that of pure gold particles.

Particularly interesting is that these Fe@Au nanoparticles are superparamagnetic with $\mathbf{T}_B \sim 42\,K$. At 300 K, no coercivity (H_c) and remanence ($\mathbf{M}_r$) are observed, while they are 728 Oe and 4.12 emu/g at 2 K, respectively (see Fig. 2.2).

The authors have also investigated self-assembly of the Fe@Au nanoparticles in a magnetic field for potential biomedical applications. The Fe@Au nanoparticles formed parallel chains with length ranging from 5 to 30 nm, and each chain can be considered as a single magnetic domain. Under the influence of the external

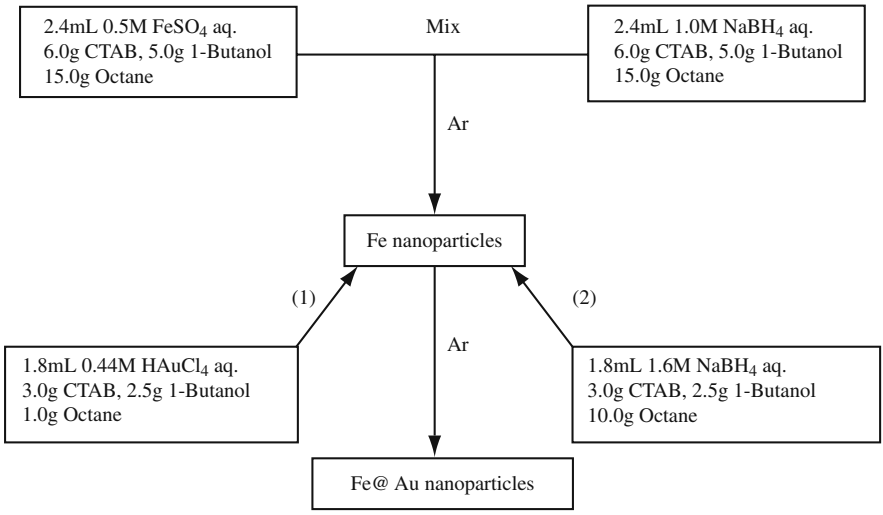

Fig. 2.1 Schematic diagram showing the reverse-micelle method for preparation of Fe@Au nanoparticles. Reproduced with permission from J. Solid State Chem. **159**, 26–31 (2001) Copyright 2001 Elsevier

magnetic field, these single domains are aligned along the direction of the magnetic field to form even longer parallel chains.

Other researchers [15, 13, 14, 63, 64, 16, 45] have also successfully fabricated different sized Fe@Au nanoparticles using the same method and characterized them with XRD, UV/vis, and TEM techniques. Zhou et al. [63] obtained the average particle size of the core–shell structure about 8 nm, with about 6 nm diameter core and 1–2 nm thick shell. Carpenter [16] synthesized nanoparticles with a 7 nm core in diameter and a 1 nm thick shell. These Fe@Au nanoparticles are found to be air stable, and their magnetic properties are enhanced.

Chen et al. [20] have synthesized gold-coated acicular and spherical iron-based nanoparticles by using a mild chemical reduction process. Iron core nanoparticles are synthesized by simultaneous thermal decomposition of $Fe(CO)_5$ and polyol reduction of $Co(acac)_3$ in dioctyl ether before coating. The acicular iron particles are coated with gold from the gentle chemical reduction of an organo-gold compound in nonaqueous solvents. TEM and alternative gradient magnetometry studies indicate that the small particles have relatively uniform coatings, while for the larger particles, many gold surfaces have been decorated. Compared with uncoated particles, gold-coated commercial iron particles show good corrosion resistance even in a 1.03 M HCl solution at 80°C for 12 h. Additionally, although the Fe@Au particles possess a very small coercivity because of slight oxidation, the magnetic moment is still larger than that of pure iron oxide.

Ban et al. [7] have successfully synthesized Fe@Au nanoparticles (about 11 nm core of Fe and 2.5 nm shell of Au) by the partial replacement reaction in a polar aprotic solvent. High-resolution transmission electron microscopy (HRTEM) studies

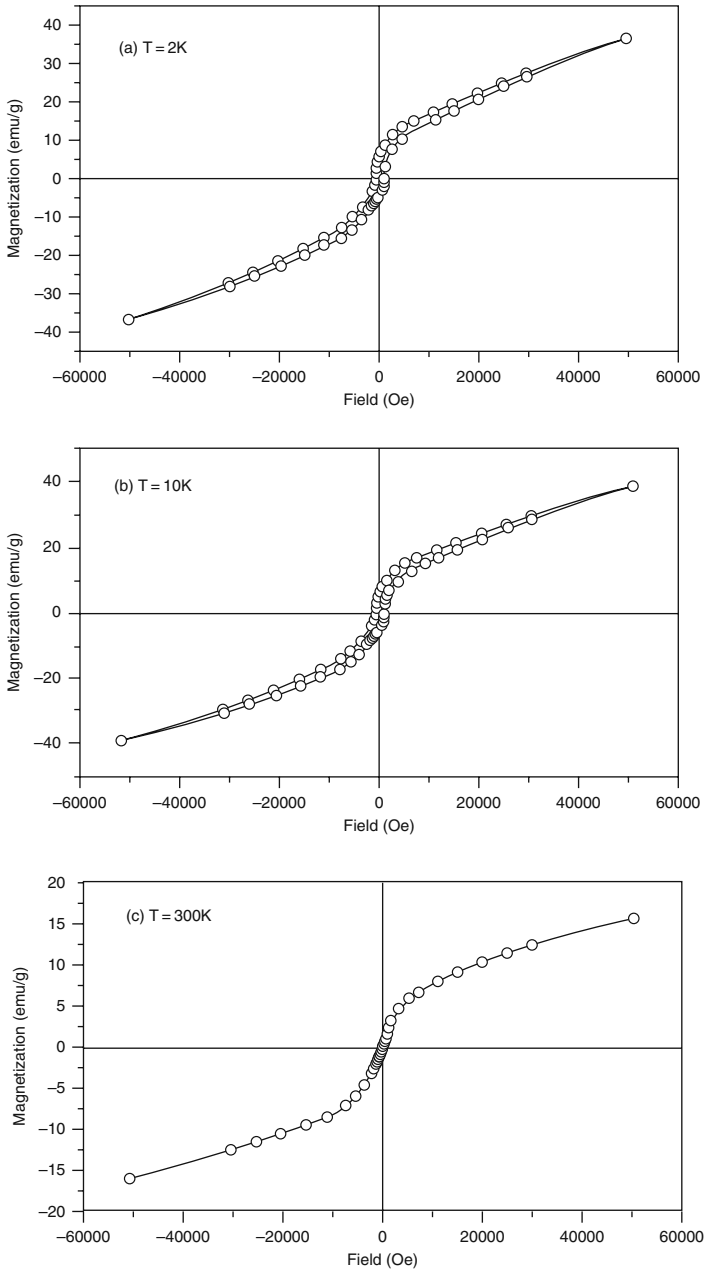

Fig. 2.2 Magnetization of Fe@Au nanoparticles vs. the magnetic field at (**a**) 2 K (**b**) 10 K, and (**c**) 300 K. Reproduced with permission from J. Solid State Chem. **159**, 26–31 (2001) Copyright 2001 Elsevier

confirm the core–shell structures with different crystal lattices: Fe (110 and 200 lattice planes) and Au (111 and 200 lattice planes). SQUID magnetometry reveals that particle magnetic properties are not significantly affected by the thickness of Au shell. The produced Fe@Au nanoparticles exhibit a red shift in absorption band as compared to pure gold nanoparticles, due to the surface plasmon resonance. Interestingly, the Fe@Au nanoparticles are ferromagnetic at room temperature.

Cho et al. [23] have reported chemical synthesis of Fe@Au nanoparticles using a reverse-micelle method through the reduction of an aqueous solution. The blocking temperature of the particles $\mathbf{T_B}$ is about 150 K, which is much higher than that of 50 K obtained by O′Connor group. A negative giant magnetoresistance effect has been observed, and the particles are metallic, which imply a metallic α-Fe core. However, the Mössbauer studies on the samples a month later have confirmed the occurrence of oxidation over time, which indicates that the Fe core is not fully covered by the Au shell or that the Au shell is permeable to oxygen. Therefore, the authors have proposed that the formation of α-Fe core Au-shell structure and subsequently the Fe core oxidizes.

Later, however, the authors have found that the structure of Fe@Au nanoparticles might be not as simple as reported earlier. To investigate the growth mechanisms and oxidation-resistant characteristics of the Fe@Au core–shell structure, Cho et al. [21] used the same synthetic method to fabricate a large enough Fe core coated with gold shell (about 19 nm). TEM, EDX, XRD, Mössbauer spectroscopy, and inductively coupled plasma studies demonstrated the Fe@Au core–shell structures and the presence of the Fe and Au phases. From atomic-resolution Z-contrast imaging and electron energy loss spectroscopy (EELS) in a scanning transmission electron microscope (STEM) studies, the Au shell grows by nucleating at selected site on the surface of the Fe core before coalescing, and the surface is rough. The authors further found that the magnetic moments of the nanoparticles, in the loose powder form, decrease over time due to oxidation (see Fig. 2.3). On the other hand,

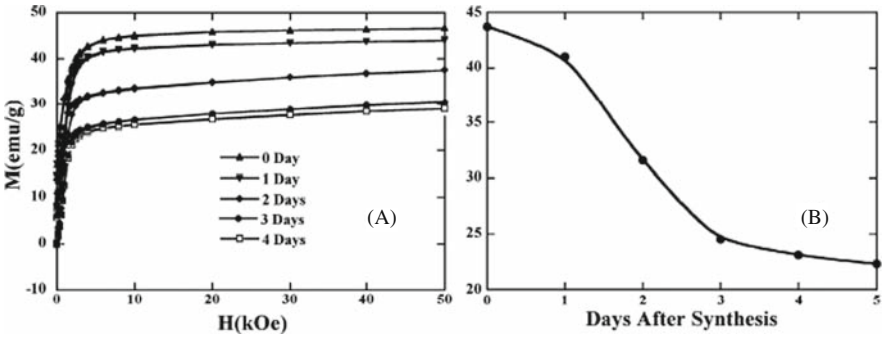

Fig. 2.3 (**A**) First quadrant of the magnetic hysteresis loop at 5 K. From the top, each curve indicates the measurement with a 1-day interval, right after synthesis. (**B**) Decay of saturation magnetization of exposed Fe/Au nanoparticles over time. Reproduced with permission from Chem. Mater., **17**, 3181–3186 (2005). Copyright 2005 American Chemical Society

electrical transport measurements showed that the particles in the pressed pellet form are fairly stable for the resistance, and magnetoresistance does not change over time.

Cho et al. [22] have further investigated the Fe@Au nanoparticles using both the conventional- and synchrotron-based X-ray diffraction and the magnetic and Mössbauer spectral techniques. The powder X-ray diffraction patterns indicate the presence of crystalline α-iron and gold and the absence of any crystalline iron oxides or other crystalline products. However, the Mössbauer spectra of both uncoated iron nanoparticles and the Fe@Au nanoparticles showed that three major iron-containing components are found (see Fig. 2.4). Of the iron components, 16% and 40% are represented by the expected α-iron phase in the uncoated and gold-coated iron nanoparticles, respectively. The other byproducts are an amorphous $Fe_{1-x}B_x$ alloy and Fe(III) oxide as well as paramagnetic Fe(II) and Fe(III) components. These results indicate that the produced Fe@Au nanoparticles through reverse micelles are far more complicated than had been believed.

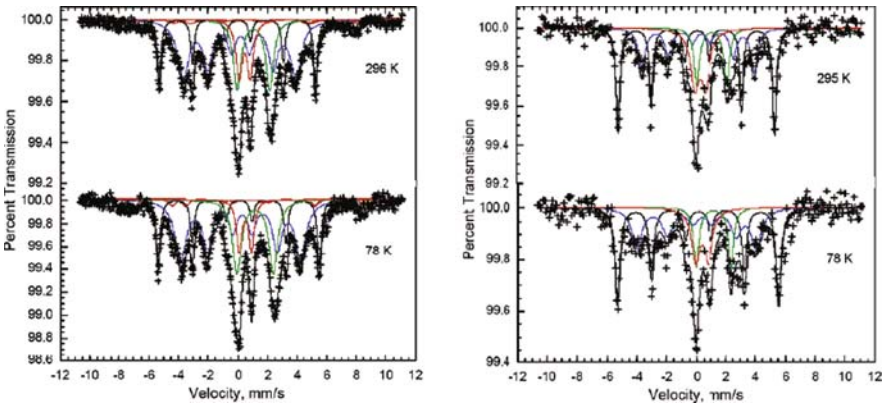

Fig. 2.4 Mössbauer spectra of the iron (*left panel*) and the Fe@Au (*right panel*) nanoparticles prepared in a reverse micelle. The Fe(II), Fe(III), R-iron, and $Fe_{0.73}B_{0.27}$ components are shown in different colors (see original article). They are obtained within a week and approximately 2 weeks after synthesis for gold-coated and uncoated iron particles. Reproduced with permission from Chem. Mater. **18**, 960–967 (2006). Copyright 2006 American Chemical Society

Zhang et al. [62] have exploited a laser ablation technique to synthesize the Fe@Au core–shell nanoparticles. This technique includes three steps. The first step is to make both the Fe core and the Au shell by using the laser ablation method separately. The second step is to prepare the Fe core through a wet chemistry method and to be subsequently coated with Au shell by laser ablation of Au powder. The third step is magnetic extraction/acid washing for sample purification. The main advantage of this fabrication technique is the second step, which provides a higher overall yield and better control of the size of the magnetic core. Their studies indicate that although the effect of irradiation is complicated, the most possible coating

process is that Au particles are fragmented into small Au clusters and deposited onto the iron core through repeated heating and melting. The laser-irradiated mixture Fe-containing nanoparticles were separated by magnetic extraction techniques, and the uncoated or incompletely Au-coated nanoparticles were washed away through acid washing. The detailed synthesized process is illustrated in Fig. 2.5.

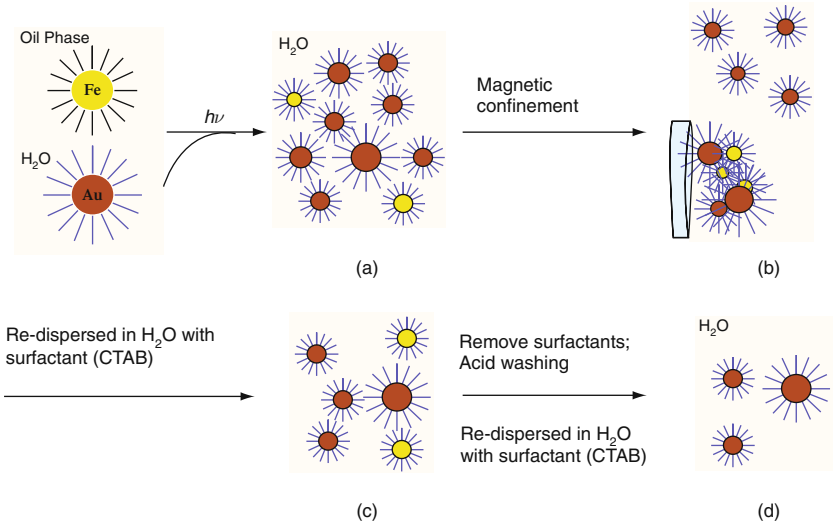

Fig. 2.5 Experimental process for fabrication of Fe@Au magnetic core–shell nanoparticles. Reproduced with permission from J. Phys. Chem. B. **110**, 7122–7128 (2006). Copyright 2006 American Chemical Society

The samples have been characterized during and up to several months after synthesis by HRTEM, HAADF STEM, EDX, XRD, UV-vis, inductively coupled plasma atomic emission spectroscopy, and SQUID magnetometry. The red-shifted and much broadened spectra are observed in the absorption band structure of the Fe@Au nanoparticles due to the surface plasmon resonance, a reflection of the shell-thickness effect. The Au shell is about 3-nm diameter with fcc structure and the lattice interplanar distance of 2.36 Å. The core is about 18-nm diameter bcc Fe single domain with the lattice interplanar distance of 2.03 Å. The nanoparticles are superparamagnetic at 300 K with a high blocking temperature $\mathbf{T}_B$ of 170 K and exhibit excellent long-term oxidation resistance. After 4 months of shelf storage in normal laboratory conditions, high-saturation magnetization is found (210 emu/g), which is about 96% of the Fe bulk value.

As discussed above, the Fe@Au nanoparticles have some unique advantages: first, they can be easily prepared in either aqueous or organic medium. Second, the particles often have high saturation magnetization, as compared with iron oxide and other magnetic material. Third, because of diverse surface functionality of gold, gold-coated iron nanoparticles have increased functionality.

2.2.2 Cobalt-Based Core–Shell Nanoclusters

2.2.2.1 Co@Pt Core–Shell Nanoalloys

Park et al. [46] have exploited redox transmetalation reaction techniques for the first time to synthesize $Co_{core}Pt_{shell}$ nanoalloys under 10 nm. As shown in Scheme 2.1, first, the Co nanoparticles are prepared from the thermolysis of $Co_2(CO)_8$ in toluene solution. Next, the $Co_{core}Pt_{shell}$ nanoparticles are synthesized by refluxing 6.33 nm Co nanoparticle colloids (0.5 mmol) and $Pt(hfac)_2$ (0.25 mmol) in a nonane solution containing 0.06 mL of $C_{12}H_{25}NC$ as a stabilizer. After 8 h of reflux, the core–shell nanoparticles are isolated from the dark red–black solution in powder form after adding ethanol and centrifugation. Last, reaction byproduct $Co(hfac)_2$ is separated from the core–shell nanoparticles.

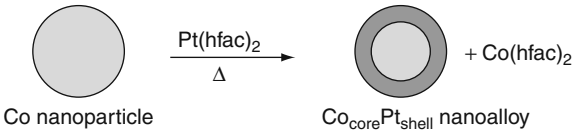

Scheme 2.1 Synthetic route of core–shell nanoalloys via modified redox transmetalation reaction. Reproduced with permission from J. Am. Chem. Soc. **123**, 5743–5746 (2001). Copyright 2001 American Chemical Society

Magnetic studies of the $Co_{core}Pt_{shell}$ nanoparticles indicate that they retain most magnetic properties of pure Co core and are not significantly affected by the Pt shell. The block temperature of this sample is about 15 K and a coercivity is 330 Oe at 5 K, which are less than the pure Co nanoparticles but are close to those of nanoparticles with similar size to the Co_{core}.

Later, Park et al. [47] have exploited a similar redox transmetalation reaction technique to fabricate similar-sized $Co_{core}Pt_{shell}$ nanostructures (Scheme 2.2) and studied their magnetic properties and thermally induced dynamic phase transition behavior.

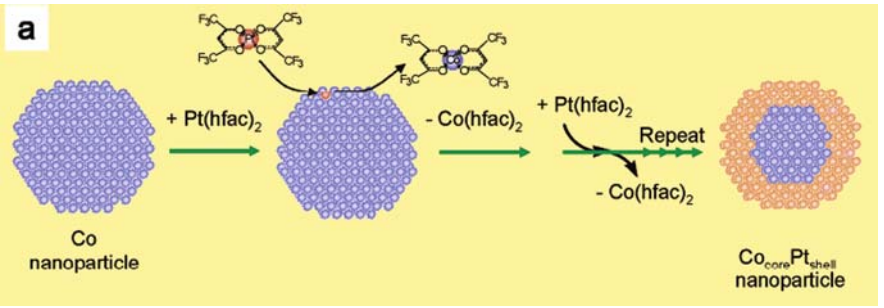

Scheme 2.2 Synthetic routes of $Co_{core}Pt_{shell}$ nanoalloys via modified redox transmetalation reaction. Reproduced with permission from J. Am. Chem. Soc. **126**, 9072–9078 (2004). Copyright 2004 American Chemical Society

The $Co_{core}Pt_{shell}$ nanoparticles are superparamagnetic with zero magnetic coercivity (H_c) at room temperature, and 330 Oe at 5 K. In particular, the H_c is considerably improved to 1300 and to 7000 after the $Co_{core}Pt_{shell}$ nanoparticles are annealed at 600 and 700°C for 12 h. Moreover, the particle annealed at 700°C shows ferromagnetism with an H_c of 5300 Oe at room temperature (Fig. 2.6).

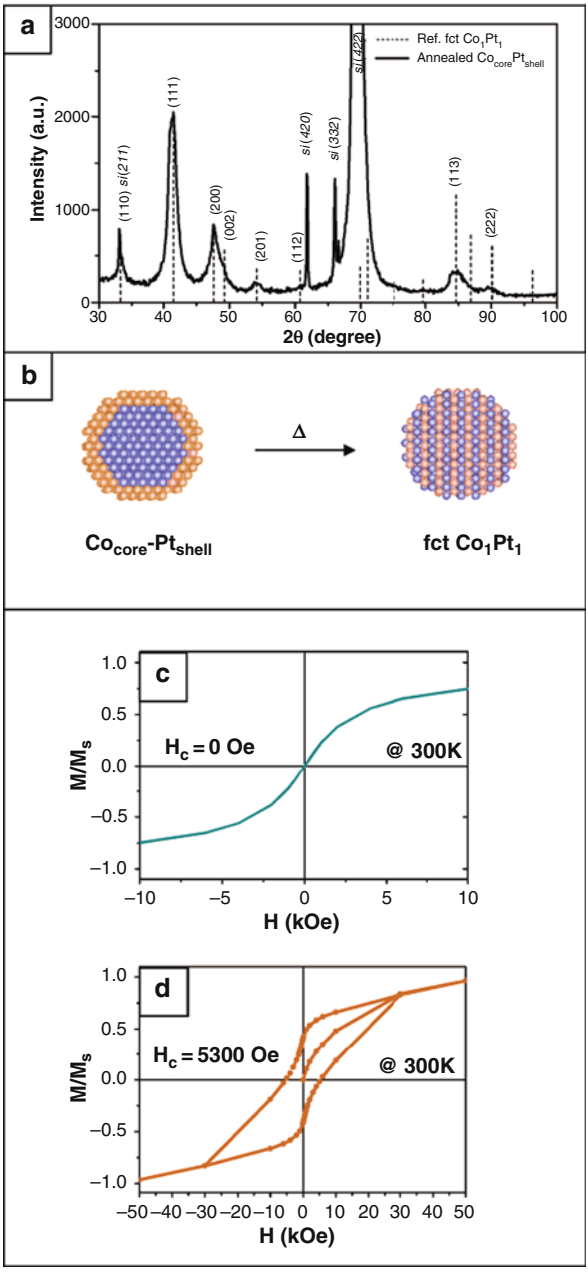

Fig. 2.6 XRD analysis and magnetic properties of $Co_{core}Pt_{shell}$ nanoparticles. (**a**) XRD pattern of $Co_{core}Pt_{shell}$ nanoparticles annealed at 700°C for 12 h. All peaks are well matched to reference fct Co_1Pt_1 alloys (dashed line). (**b**) Thermal alloying of $Co_{core}Pt_{shell}$ nanoparticles to anisotropic fct structure. Hysteresis loops of $Co_{core}Pt_{shell}$ nanoparticles measured at 300 K (**c**) before and (**d**) after the annealing process at 700°C. The magnetic coercivity of the nanoparticles is significantly enhanced from 0 to 5300 Oe, exhibiting room-temperature ferromagnetism. Reproduced with permission from J. Am. Chem. Soc. **126**, 9072–9078 (2004). Copyright 2004 American Chemical Society

Jun et al. [34] have demonstrated Co@Pt core–shell nanoparticles can be effectively served as a bifunctional nanoplatform for the hydrogenation of a number of unsaturated organic molecules under mild conditions, and also for the magnetic separation and recycling ability. They also prepared Co@Pt nanoparticles via the redox transmetalation reaction process between $Pt(hfac)_2$ and cobalt particles. The platinum shell surface is stabilized by dodecyl isocyanide capping molecules (Fig. 2.7). The average particle size is 6.4 nm, while the diameter of a cobalt core is 4.6 nm; the overall stoichiometry is $Co_{0.45}Pt_{0.55}$. Elemental analysis and HRTEM study indicate that the thickness of the Pt layer is about ~0.9 nm, corresponding to ~4 layers of Pt. The core–shell nanoparticles exhibit superparamagnetic behavior at room temperature with the blocking temperature $\mathbf{T}_B \sim 15\ K$ and a coercivity $H_c \sim$ 660 Oe at 5 K

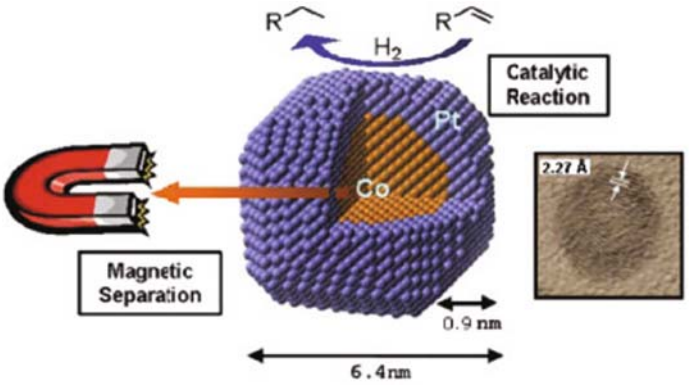

Fig. 2.7 The dual functionality of Co@Pt core–shell nanoparticles. Insert: The HRTEM image of a single nanoparticle. The 2.27 Å represents the lattice constant of the Pt shell. [35] – *Reproduced by permission of The Royal Society of Chemistry*

2.2.2.2 Co@Au, Co@Pd, Co@Pt, and Co@Cu Nanoparticles

Lee et al. [39] have successfully fabricated Co@Au, Co@Pd, Co@Pt, and Co@Cu core–shell nanostructures by using the redox transmetalation reaction technique. During the transmetalation processes, metal ions M_{II}(M_{II} = Au^{3+}, Pd^{2+}, Pt^{2+}, or Cu^{2+}) of the reactant metal complexes ($M_{II} - Li$) are reduced on the surface of M_I (M_I = Co in this work) nanoparticles, while neutral M_I(Co) atoms are oxidized to $M_I{}^{y+}$(Co^{2+}) accompanying the formation a Co–ligand complex ($M_I - L_j$) as a resultant reaction byproduct (Scheme 2.3). Repeating this process leads to a complete covering of Co core by M_{II} shell layers. The advantage of this technique is that the original Co nanoparticles are retained because of shell layer formation and core metal consumption occur simultaneously.

EDS studies indicate that the nanoparticle is estimated to have a 5.7 nm Co core and 0.4 nm Au shell with Co/Au ratio of 79:21 for Co@Au; 4.9 nm Co core and

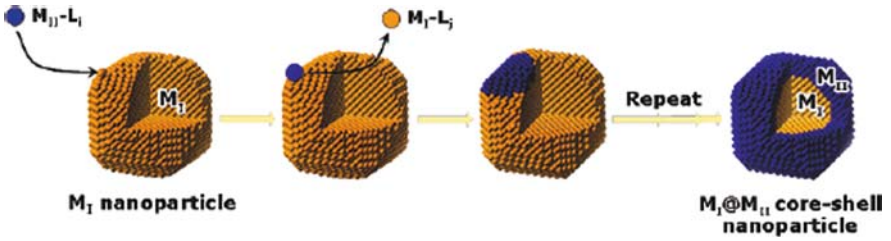

Scheme 2.3 Schematic of core–shell nanoparticle formation via redox transmetalation processes. Reproduced with permission from J. Am. Chem. Soc. 127, 16090–16097 (2005). Copyright 2005 American Chemical Society

0.9 nm Pd shell with Co/Pd ratio of 47:53 for Co@Pd; the Co/Pt ratio of 45:55 with 4.6 nm Co core and 0.9 nm Pt shell for Co@Pt; and 5.2 nm Co core shell and 0.7 nm Cu shell with the ratio of 54:46 for Co@Cu nanostructure. The HRTEM studies further confirm the formation of the shell of Au, Pd, Pt, and Cu on Co nanoparticles by their good coincidence with the corresponding lattice parameters for their fcc (111) plane.

SQUID magnetometer measurements are performed on these core–shell structures and show coercivity (H_c) of 2090 Oe for pure Co nanoparticles, 1310 Oe for Co@Au, 840 Oe for Co@Cu, 660 Oe for Co@Pt, and 740 Oe for Co@Pd core–shell nanoparticles, respectively (Fig. 2.8). Taking into account that average diameter of cobalt for Co, Co@Au, Co@Cu, Co@Pt, and Co@Pd is estimated to be 6.5, 5.7, 5.2, 4.7, and 4.9 nm, respectively, the H_c trend suggests that core–shell nanoparticles with larger Co core sizes have higher coercivity. Therefore, the magnetism of the core–shell nanoparticles mainly stems from the magnetic core while the noble metal shell layer has little effect on it. Superparamagnetic behavior is observed for all of these nanoparticles at room temperature.

2.2.2.3 Pt@Co Core–Shell Nanoclusters

Sobal et al. [54] have developed a new two-stage route to synthesize monodisperse, controllable Pt@Co core–shell structures. The first step is to prepare definite diameter pure platinum particles. The second step involves thermal decomposition of cobalt carbonyl on the Pt seeds. The thickness of the Co shell can be controlled by varying the amount of dicobalt dicarbonyl. For the ratio Pt:$Co_2(CO)_8$ 1:4, the average diameter of the spherical bimetallic particles is 7.5 nm with the maximum thickness of Co (2.3±0.2 nm). In the case of Pt/$Co_2(CO)_8$ 1:5, incomplete coverage was observed due to cobalt island formation on the platinum surface. The particles exhibit superparamagnetic behavior at room temperature, and the blocking temperature $\mathbf{T_B}$ is between 175 and 225 K.

2.2.2.4 Co@Cu Core–Shell Nanoclusters

Guo et al. [30] have fabricated Co@Cu core–shell nanoparticles by using a displacement method in aqueous solution at room temperature. The nanoparticles

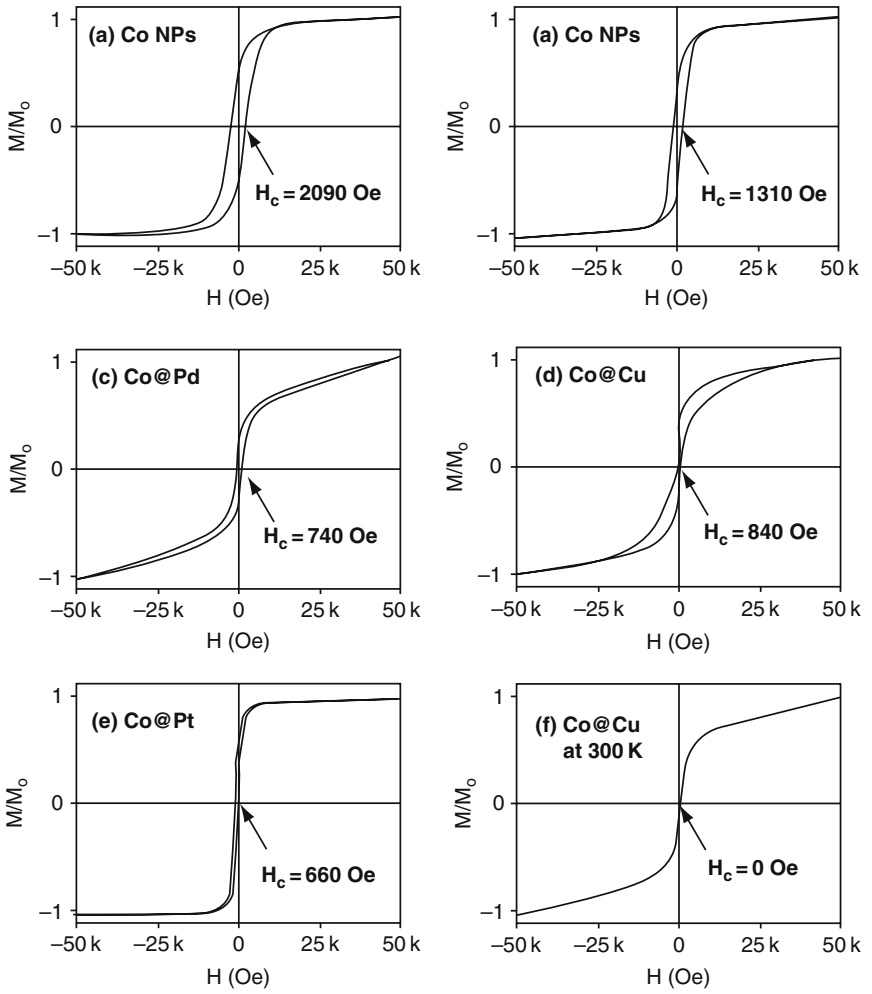

Fig. 2.8 Hysteresis loops of (**a**) Co nanoparticles and core–shell nanoparticles (**b**) Co@Au, (**c**) Co@Pd, (**d**) Co@Cu, and (**e**) Co@Pt at 5 K on a SQUID magnetometer. (**f**) Hysteresis loop of Co@Cu nanoparticles at 300 K shows superparamagnetism. Reproduced with permission from J. Am. Chem. Soc. 127, 16090–16097 (2005). Copyright 2005 American Chemical Society

were fabricated through a wet chemical scheme by using the surfactant sulfobetaine, dodecyldimethyl (3-sulfopropyl) ammonium hydroxide (98%) in tetrahydrofuran. Cobalt oxide was not present in the nanoparticles upon exposure to air through X-ray absorption near-edge structure analysis. The relative high blocking temperature ($\mathbf{T}_B \sim 235\,K$) was found for the Co@Cu nanoparticles, indicating the coating enhanced the magnetic properties of the nanoparticles.

2.2.2.5 Co@Ag Core/Shell Nanoclusters

Sobal et al. [54] have fabricated monodisperse bimetallic Ag@Co core–shell nanoparticles by using colloid chemistry methods. These nanoparticles exhibit optical and magnetic behavior significantly different from that of pure Ag and Co metals. In addition, the presence of a noble metal appears to improve the stability of nanosized Co against oxidation.

Rivasa et al. [50] have prepared Co@Ag nanoparticles through a microemulsion method in an inert atmosphere. The size of the nanoparticles is controlled by the water droplets of the microemulsions. This whole procedure can be divided to two steps. The first step is to produce the magnetic core by mixing two water-in-oil microemulsions containing the reactants dissolved in the aqueous phase. The second step is to coat the core with Ag through successive reactions in microemulsions. The reaction takes place inside the droplets, which controls the final size of the particles. Subsequently, silver ions are adsorbed onto these particles and finally are reduced to produce a silver shell. The produced samples contain 3.3–40.5 vol% Co, and the average size of the particles is about 15–60 nm.

The authors have also investigated the temperature dependence of the magnetization and found that the magnetic properties are strongly dependent on the annealing temperature. The study shows coercive fields as high as $H_c = 600$ Oe at room temperature after thermal treatments (TA $\approx 500\,\mathrm{deg}\,C$).

Later, Rivasa et al. [51] have synthesized Co@Ag core–shell nanoparticles with the same technique and explored magnetic behavior vs. heat treatment. This study confirms that under the experimental conditions, the size of the Co nuclei is determined by the reactant concentration, whereas microemulsion droplet size controls the Ag covering.

2.2.2.6 Co@Au Core–Shell Nanoclusters

Paulus et al. [48] have presented a detailed experimental study of Co colloidal particles stabilized by organic ligands with and without gold coating. The magnetic anisotropy of the Co@Au particles was found to be highly reduced, to a value very close to the bulk.

Xu and Wang [61] have fabricated Co@Au core–shell nanoparticles directly from gas phase by using a physical-vapor-deposition-based nanocluster deposition technique. The synthesized Co–Au nanoparticles are Co82.7Au17.3 at.% with the size ranging from 5 to 15 nm in diameter and an average size of about 12 nm. The composition ratio in the particles can be adjusted by changing the ratio of sputtered areas of Co and Au in the target. The advantage of this method is that it can precisely control conditions for particle formation, thus good control of phase, size, and size distribution of particles.

Low-temperature and room-temperature hysteresis loops show that the Co–Au nanoparticles retain the magnetic properties of pure Co core. At room temperature, the Co–Au nanoparticles show superparamagnetic behavior with a very high blocking temperature $\mathbf{T}_\mathrm{B} \sim 290\,K$. A field-cooled low-temperature hysteresis loop

of Co–Au nanoparticles at 50 K indicates the existence of oxide, and Au shell does not fully cover the Co core.

To avoid the formation of the interface between the core and the shell in the redox transmetalation reaction process, Bao et al. [9] have synthesized Co–Au core–shell nanoparticles by using an organo-gold compound as precursor in a nonpolar solvent. No diffraction pattern of cobalt oxide was observed in XRD, which confirmed that these produced Co–Au core–shell nanoparticles are stable in organic solution and last up to several months. However, their stabilities are reduced in aqueous solution, which are mainly caused by the reaction of cobalt and thiol groups.

TEM, HRTEM, and Z-contrast imaging studies show that the core–shell structure is about 9 nm and a single-crystal Co core is surrounded by multiple gold grains, forming a raspberry structure, and the core diameter is 5–6 nm, close to the size of the cobalt seeds used during synthesis, and the shell is roughly 1.5–2.0 nm thick. The particles are superparamagnetic at room temperature and the blocking temperature $\mathbf{T}_B$ is about 55 K. The UV-visible absorption spectra of these nanoparticles show a red shift to 680 nm because of the surface plasmon resonance enhanced absorption.

2.2.3 Ni-Based Core–Shell Nanoclusters

2.2.3.1 Ni@Pd Core–Shell Nanoclusters

Sao-Joao et al. [53] have successfully fabricated Pd–Ni core–shell nanoparticles with the average size (5–7 nm) through decomposition of metalorganic compounds. TEM, EDS, HRTEM, energy-filtered microscopy (EFTEM), and XPS studies indicate that the physical and chemical properties of the Pd shell are sensitively dependent on its electronic properties, which are influenced by the presence of the Ni core and by the deformation in the Pd lattice. The catalytic properties of the pure metal and the bimetallic particles, toward CO oxidation, have been investigated. The core–shell clusters show similar catalytic activities toward the CO oxidation as the case of pure Pd clusters, i.e., no increase of reactivity is observed on the Ni@Pd core–shell structure, which might be caused by the presence of edges in the small particles.

2.2.3.2 Ni@Ag Core–Shell Nanoclusters

Chen et al. [19, 38] have successfully fabricated Ni@Ag core–shell nanoparticles by successive hydrazine reduction of metal salts in ethylene glycol without the addition of protective agents. To prohibit the particles from coalescing, the appropriate nickel concentration for the coating of Ag nanoshells should be less than 1.0 mm. The TEM and XPS on surface composition studies indicated that Ni cores are fully covered by Ag nanoshells, and the shell thickness could be controlled by the silver nitrate concentration. The EDP and XRD analyses reveal that both Ni cores and Ag shells have an fcc structure.

Later, Chen et al. [38] have further developed this synthetic technique by using polyethyleneimine (PEI) as a protective agent to fabricate Ni-core/Ag-shell

(Ni@Ag) nanoparticles. The produced Ni@Ag nanoparticles are monodisperse, and the core is about 6.2 nm in diameter, and the shell thickness is about 0.85 nm. In the nickel concentration of 0.25–25 mM, the size of the Ni@Ag nanoparticles shows no significant change for different thickness of Ag coating. X-ray photoelectron spectroscopy indicates both Ni cores and Ag shells have an fcc structure, and the Ni cores are fully covered by Ag shells. Moreover, a peak was observed at 430 nm in the absorption band of the Ni@Ag nanoparticles, which is consistent with the characteristic spectra of Ag nanoparticles. The sample is nearly superparamagnetic. The saturation magnetization (M_s), remanent magnetization (M_r), and coercivity H_c are 17.2 emu g^{-1}, 4.0 emu g^{-1}, and 81 Oe, respectively, based on the weight of Ni cores. The coating of Ag shells leads to a decrease of M_s and M_r, which indicates that the formed Ni–Ag interface plays a quenching role on the magnetic moment. The thermal and XRD analyses indicate that the Ag shells provide a better antioxidation protection to Ni@Ag nanoparticles as compared to the case of pure Ni nanoparticles.

2.2.3.3 Ni@Au Core–Shell Nanoclusters

Chen et al. [18] have developed a redox transmetalation method by combining with a reverse-microemulsion technique to synthesize Ni–Au core–shell nanoparticles. The obtained size of the nanoparticles ranges from 15 to 30 nm in diameters, with 5–10 nm core diameters and 5–10 nm shell thickness. A red-shift absorption to 590 nm was observed in this core–shell structure as compared to pure gold nanoparticles due to the enhanced surface plasmon resonance absorption. The blocking temperature of the nanoparticles is 16 K, and the superparamagnetic behavior was detected at room temperature. The saturation magnetization, remanent magnetization, and coercivity at 5 K are 9.0 emu/g, 4.1 emu/g, and 2 kOe, respectively, which are dramatically smaller than that of 55 emu/g at 300 K for bulk nickel metal. This reduction in moment might stem from the small size effect, the oxidation of the Ni cores, the increased surface of the nanoparticles, the crystal lattice defects, etc.

2.3 Theoretical Studies of Bimetallic Magnetic Core–Shell Nanoclusters

In contrast to extensive experimental studies of bimetallic core/shell nanostructures, theoretical studies are much less (Table 2.1). In this section, we will give a more detailed survey on previously reported theoretical results.

2.3.1 Iron-Based (Fe@Au) Core–Shell Nanoclusters

Sun et al. [56] have reported the first theoretical study of gold-coated iron nanoclusters using a gradient-corrected density functional theory (DFT). Specifically,

the authors used a combination of the Becke exchange functional and the Perdew–Wang correlation functional (BPW91), and a plane-wave basis set with the projector augmented plane-wave (PAW) method. The authors focused on the effect of gold coating on the structural and magnetic properties of the iron core of various sizes, as well as chemical reaction of uncoated and coated iron clusters with oxygen.

Calculated magnetic moments of clusters $Fe_1@Au_1$, $Fe_1@Au_{12}$, and $Fe_1@Au_{12}@Au_{30}@Au_{12}$ (Fig. 2.9) are 3.44, 3.0, and 3.0 μ_B, respectively. These values are all greater than the bulk value of 2.2 μ_B/atom, indicating that the gold shells provide an enhancement effect on the magnetism of iron atom.

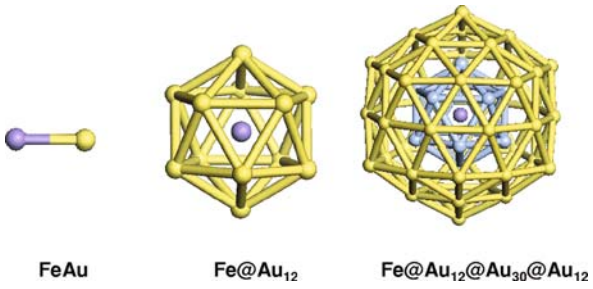

Fig. 2.9 Geometries of Fe atom enclosed in gold shells. Reproduced from [57]. Copyright (2006) by the American Physical Society

The authors have also examined whether a Fe_{13} core can remain magnetic with a gold shell of two different thicknesses, namely, $Fe_{13}@Au_{42}$ and $Fe_{13}@Au_{134}$. Main results of their calculation for Fe_{13}, $Fe_{13}@Au_{42}$, and $Fe_{13}@Au_{134}$ are given in Table 2.2. For $Fe_{13}@Au_{42}$, the lowest-energy structure is an icosahedron with I_h symmetry, although bare Fe_{13} itself is a distorted icosahedron, which indicates that the gold coating results in a structural change of the iron core. Meanwhile, the magnetic moment of the Fe_{13} core is more or less preserved even though the Fe–Fe bond length is expanded by 3.2% with the gold coating. Covering additional gold shells to $Fe_{13}@Au_{42}$ has little effect on the bond length and magnetic moment of the Fe_{13} core. The induced magnetic moment within the Au shell is mainly at the Au/Fe interfacial layer, and the outermost Au layer shows no magnetic moment. Hence, the thickness of the gold shell has a negligible effect on the magnetic moment of the Fe_{13} core and little influence on the induced moment within the gold coating.

Sun et al. have also studied the oxidation of Fe_{13} and $Fe_{13}@Au_{42}$ nanoclusters and found that O_2 dissociates and the atomic O binds strongly with the outer Fe atoms with a binding energy of 8.04 eV. The total magnetic moment of $Fe_{13}O_2$ is 38 μ_B, less than that of the pure Fe_{13}. As for $Fe_{13}@Au_{42}$, oxygen remains molecular, and the adsorption energy of O_2 to the cluster is small (< 0.25 eV), indicating that gold coating prevents the iron core from oxidation.

Table 2.2 Bond lengths (in Å) and magnetic moment (in μ_B) of Fe_{13} and the Fe@Au core–shell nanoclusters. Reproduced from [56]. Copyright (2006) by the American Physical Society

	Fe_{13}	$Fe_{13}@Au_{30}@Au_{12}$	$Fe_{13}@Au_{30}@Au_{12}@Au_{60}@Au_{12}$
μ_{Fe1}	2.32	2.384	2.357
μ_{Fe2}	3.00	2.923	2.801
μ_{Au}		0.018 (1st shell)	0.015 (1st shell)
		0.014 (2nd shell)	0.012 (2nd shell)
			0.010 (3rd shell)
			0.007 (4th shell)
			0.003 (5th shell)
R_{Fe1}	2.390	2.457	2.438
R_{Fe2}	2.512	2.594	2.543
R_{Fe-Au}		2.830	2.820

2.3.2 Cobalt-Based Core–Shell Nanoclusters

2.3.2.1 Co@Cu, Co@Ag Core–Shell Nanoclusters

Guevara et al. [29] have explored electronic and magnetic properties of Co cluster coated with Cu and Ag ($Co_N X_M$, X = Cu, Ag, and $N + M$ up to 405) using a parametrized tight-binding Hamiltonian method. The noble-metal coating has the structure of an fcc lattice. In the case of Co@Cu clusters, both the average and the total magnetic moments show an oscillatory behavior as a function of coating thickness, as shown in Fig. 2.10. Because of hybridization with the Cu atoms, the moment of the core–shell cluster is attenuated in comparison with the bare Co_{13} cluster. For some special coatings, Cu is antiferromagnetic (AFM) to Co and thus yields smaller magnetic moment per Co atom, and in some cases even smaller than that of bulk Co. They also found that a rather open or corrugated cluster surface induces a ferromagnetic polarization.

For the Co@Ag core–shell clusters, the total magnetic moment depends not only on the number of Co atoms but also on the number of surrounding Ag atoms as well as the shape of the Ag shell, as shown in Fig. 2.11. Moreover, Guevara et al. have found that the spin on Ag is antiparallel to that on Co for various coatings, thereby giving smaller total magnetic moment of the core–shell clusters than that of pure Co clusters. In contrast to the Cu coating, the magnetization of Co core per atom within the Ag coating is larger than that of bulk Co value. A few cases of ferromagnetic polarization are also identified and these are due to a corrugated outer Ag shell with several poorly coordinated Ag atoms (spikes).

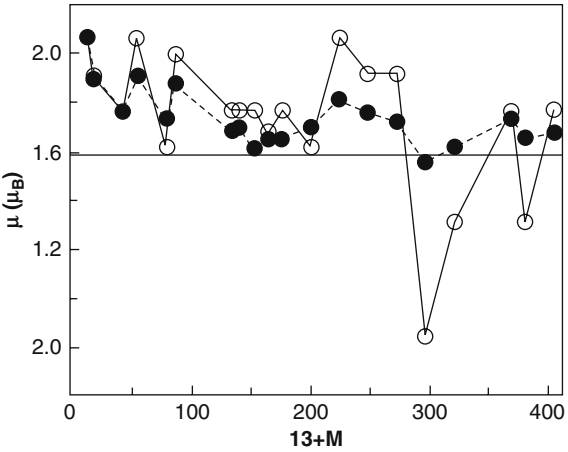

Fig. 2.10 Magnetic moment per Co atom vs. increasing number of Cu atoms for $Co_{13}Cu_M$ clusters. O corresponds to the total magnetic moment, • to the magnetic moment of the Co core. Reproduced from [29]. Copyright (1998) by the American Physical Society

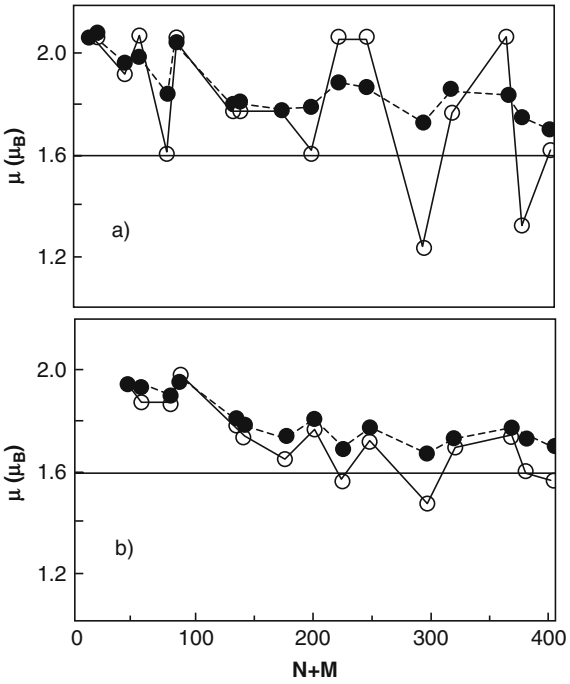

Fig. 2.11 Same as Fig. 2.10 for (**a**) $Co_{13}Ag_M$ and (**b**) $Co_{43}Ag_M$ clusters. Reproduced from [29]. Copyright (1998) by the American Physical Society

2.3.2.2 Pd@Ag, Ni@Ag, Ni@Au, Co@Au Core–Shell Nanoclusters

Baletto et al. [3–6] have investigated the growth of Pd@Ag and Ni@Ag core–shell structures using molecular dynamics simulation and empirical many-body potentials derived within the second-moment approximation to the tight-binding model. Their

studies suggest that very stable core–shell structures can form over a wide range of temperatures. A novel multi-shell *A*–*B*–*A* structure can also form by inverse deposition of *B* atoms above *A* cores. The growth of *A*–*B*–*A* structures depends on the structure of the initial *A* core and the temperature. If the initial *A* core is an fcc cluster, the *A*–*B*–*A* multi-shell structures can be achieved for all three bimetallic systems (Ni/Ag and Pd/Ag) in different temperature ranges. On the contrary, the *A*–*B*–*A* structures cannot form by deposition on the I_h cores, where normal core–shell structures grow instead. The growth of the intermediate *B* shell is triggered by the fact that the most favorable positions for isolated *B* impurities inside *A* clusters are located just one layer beneath the cluster surface.

Rossi et al. [52, 28] have identified a new family of magic-number polyicosahedral core–shell clusters, Ni@Ag, by using a genetic algorithm coupled with DFT calculation (Fig. 2.12). The authors have demonstrated that these core–shell clusters are very stable on basis of energetic, electronic energy gap, and thermodynamic information. More interestingly, these core–shell clusters can have higher melting points than the corresponding pure clusters.

Several other theoretical studies have shown that Ag–Co, Au–Ni, and Au–Co particles tend to form core–shell structures, while Ag–Pd and Au–Cu tend to mix in

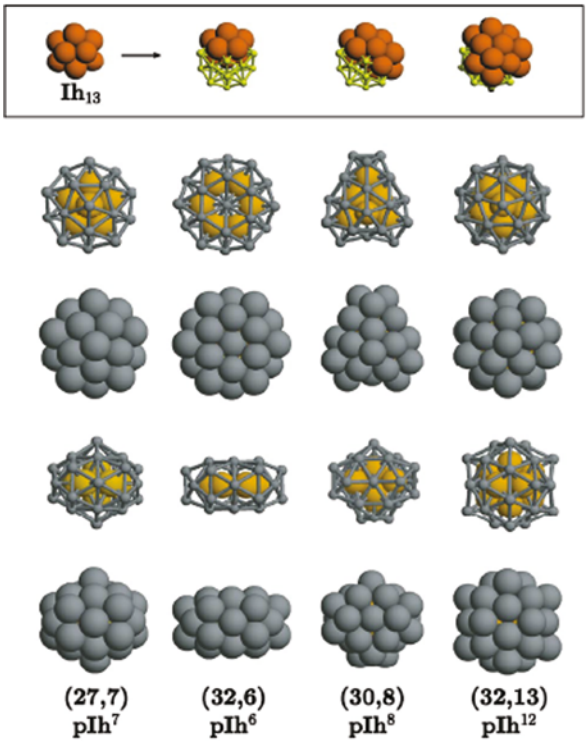

Fig. 2.12 Magic-number core–shell pI_h clusters. Reproduced from [52]. Copyright (2004) by the American Physical Society

bulk alloy phases. Many calculations have also shown that magnetic effects destabilize the core–shell arrangement of Ag–Co and Au–Co bimetallic clusters.

Hoof et al. [32] have employed Metropolis Monte Carlo and molecular mechanics methods and embedded atom potentials to study the structural and thermodynamic equilibrium states of isolated Ag–Co nanoparticles with the size ranging from 200 to 3000 atoms and temperature ranging from 0 to 1500 K. The authors have obtained a lower and an upper limit to the Co concentration for the occurrence of core–shell structure. The lower limit is determined from the balance between Co–Co binding interaction and the stress of the Ag lattice. The upper limit is associated with the wetting of the Co core by Ag shell. In the core–shell structure, the Co core expands within 2% while the Ag lattice contracts. The Co core melts at a temperature <1500 K, and the melting is insensitive to the thickness of the Ag shell. Since the melting temperature of the Ag shell is fairly lower than that of the Co core, a solid core covered by a liquid shell can be observed. The coexistence of a liquid layer and a solid center is found within the Co core, and the thickness of the liquid layer increases with increasing the temperature. As the temperature is increased, the Ag shell may undergo a crystal to amorphous transition followed by an amorphous to liquid transition, depending on its thickness. A detailed melting process is shown in Fig. 2.13, where the disordering of the core starts at the interface and proceeds toward the center as the temperature is increased.

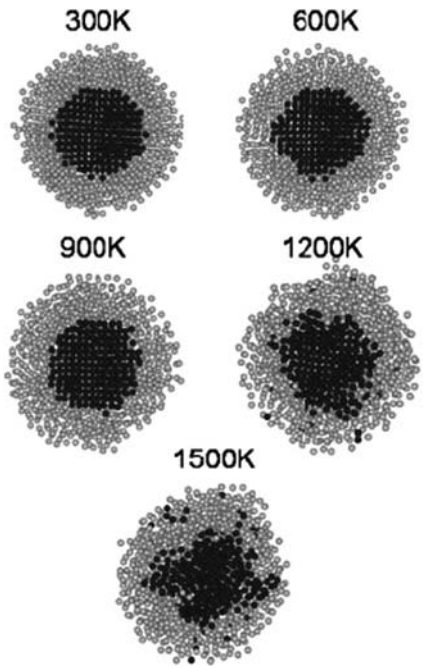

Fig. 2.13 Cuts through equilibrium $Ag_{2250}Co_{750}$ cluster configurations at several temperatures. Dark spheres: Co atoms; light spheres: Ag atoms. Reproduced from [32]. Copyright (2005) by the American Physical Society

Hou and coworkers [27, 65] have shown that the equilibrium atomic configurations of Ag–Co and Cu–Co are determined by the binding and interfacial configuration energies. Thermal vibrational entropy plays an important role in the balance of energy contributions to thermodynamic equilibrium. Core–shell Ag–Co and "onionlike" Cu–Co equilibrium configurations were observed, which can be altered by adjusting composition and temperature.

Hou and coworkers [26, 57] have also explored the slowing down process (deposition) of $Co_{285}Ag_{301}$ nanoclusters on an Ag (100) substrate using classical molecular dynamics simulation. The kinetic energies of the nanoclusters range from 0.25 eV to 1.5 eV per atom to mimic the low-energy cluster beam deposition and aerosol-focused beam techniques. Initial $Co_{285}Ag_{301}$ has a core–shell structure with one complete Ag monolayer covering the Co core. The cluster undergoes partial accommodation and partially retains a "memory" of its initial morphology. As a result of the impact, the substrate undergoes significant damage, while the degree of damage depends on the slowing down energy.

Using the same simulation methods, the authors extended their study to clusters with no special morphology when deposited on the Ag (100) surface. The effect of size and deposition energy was systematically examined. The authors have found that the interface formed between the Ag matrix and the core–shell Co@Ag nanoclusters is no more than a few atomic layers thick and that both the cobalt core and the silver shell display limited epitaxy with the substrate. The effect is not much energy dependent but is strong for the Ag shell than for the Co core.

Dorfbauer et al. [25] have explored structures of Co_xAg_{1-x} nanoparticles (864 atoms, 2.8 nm) by using molecular dynamics simulation with an embedded atom potential. Starting from a completely random distribution of Co and Ag atoms, the clusters are heated up to 1300 K and then cooled down to form Co core and Ag shell structures. Radial distribution function (RDF) analysis suggests the coexistence of both hcp-like and fcc-like stackings in the Co core.

We [58] have recently explored the structure and magnetic properties of gold-coated Co_{13} icosahedral anionic clusters $[Co_{13}@Au_{20}]^-$ using a gradient-corrected DFT. First, we searched for the lowest-energy states of the uncoated $Co_{13}{}^-$ and gold-coated $[Co_{13}@Au_{20}]^-$ clusters over a broad range of total spin magnetic moment S_z values, from 2 to 38 μ_B. Main results are summarized as follows: The $[Co_{13}@Au_{20}]^-$ anion cluster is a perfect I_h structure (Fig. 2.14). The Co–Co,

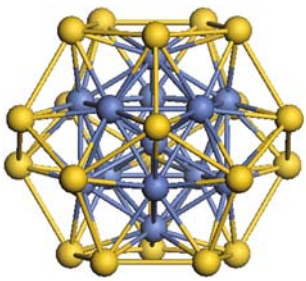

Fig. 2.14 Optimized geometry of $[TM_{13}@Au_{20}]^-$, TM=Mn and Co. Dark color represents the TM core, while light color depicts the goal shell

Co–Au, and Au–Au bond lengths in the lowest-energy structure are 2.45, 2.61, and 2.89 Å, respectively. These bond lengths can vary, depending on the total magnetic moment. In general, the Co–Co and Au–Au bond lengths increase as the magnetic moment increases, while the Co–Au bond lengths display a complicated variation pattern although in the higher magnetic states the bond lengths are usually longer.

More interestingly, the magnetic moment of $[Co_{13}@Au_{20}]^-$ is significantly reduced compared to the bare Co_{13}^-, that is, from 30 to 20 μ_B with the gold coating, 33% less than the optimal value (30 μ_B) of the bare Co_{13}^- (see Fig. 2.15). This result indicates that the gold coating can have an attenuation effect on the magnetism of strongly magnetic clusters. Paulus et al. [48] have also found the magnetic anisotropy of the Co@Au particles being greatly reduced, to a value very close to the bulk.

Mullliken population analysis on Co_{13}^- and $[Co_{13}@Au_{20}]^-$ confirms that the main magnetic moment of $[Co_{13}@Au_{20}]^-$ originates from the contribution of Co

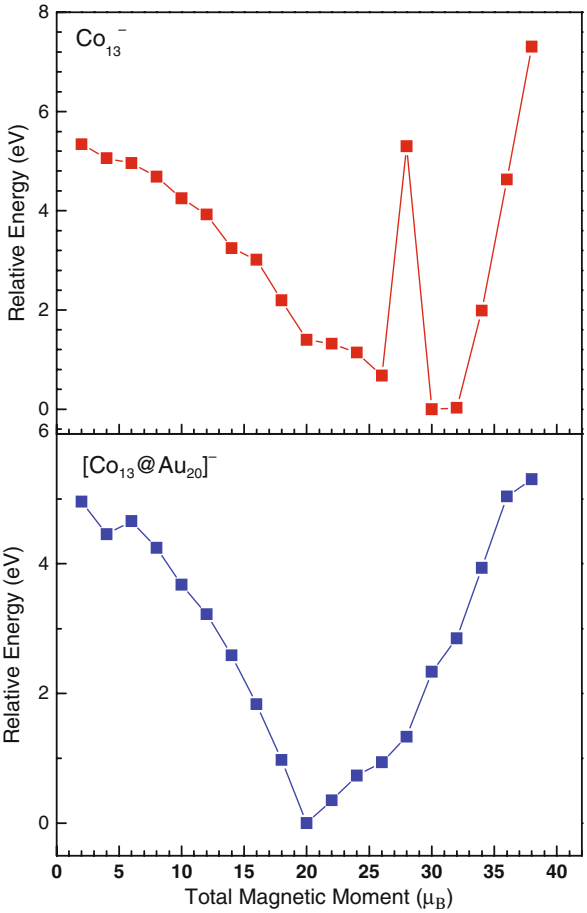

Fig. 2.15 Energies of Co_{13}^- and $[Co_{13}@Au_{20}]^-$ in different spin states referred to the respective lowest-energy states

atoms. The local atomic spins on each Au atom are nearly zero, but close to 2.0 μ_B on each Co atom. The Co atoms are ferromagnetically ordered in both uncoated and gold-coated Co_{13}^-, although the moment S_z in the uncoated cluster is larger (2.33 vs. 1.59 μ_B for surface Co atoms, and 2.06 vs. 1.89 μ_B for the central Co atom). Another source for the reduction of the total S_z of $[Co_{13}@Au_{20}]^-$ is the antiparallel ordering of the spin moments of all Au atoms (0.05 μ_B per Au) with respect to the moment of the Co_{13}^- core.

2.3.3 Mn-Based Core–Shell Nanoclusters: $[Mn_{13}@Au_{20}]^-$

Using the same computational scheme [58], we have also studied the structure and magnetic properties of gold-coated Mn_{13} anionic cluster $[Mn_{13}@Au_{20}]^-$. The lowest-energy configuration of $[Mn_{13}@Au_{20}]^-$ is a slightly distorted icosahedral structure (C_s) with a very large total S_z of 44 μ_B (see Fig. 2.16). The low spin state with the total S_z of 2 μ_B at the same symmetry (C_s) is the second lowest-energy

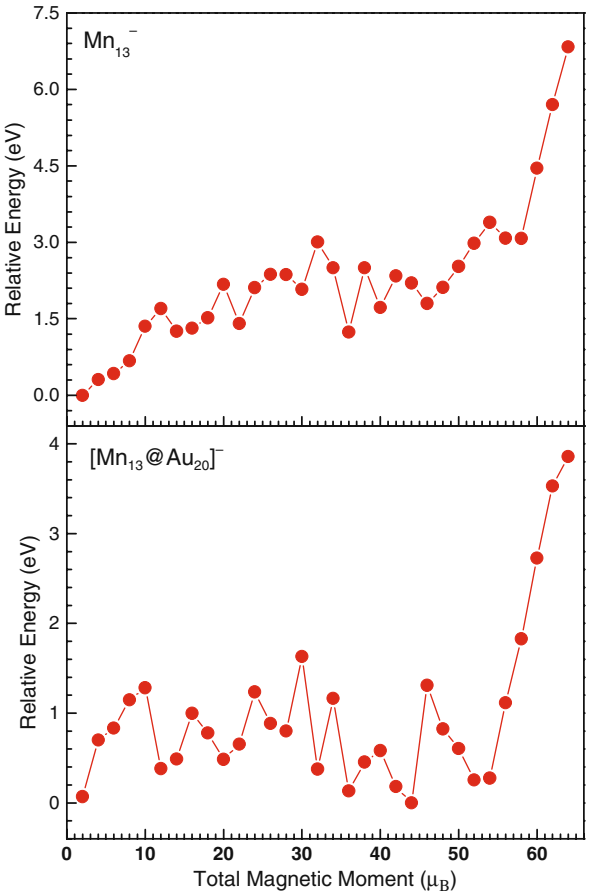

Fig. 2.16 Energies of Mn_{13}^- and $[Mn_{13}@Au_{20}]^-$ in different spin states referred to the respective lowest-energy states

configuration whose energy is only 0.071 eV higher. Other high spin states such as $S_z = 36, 42, 52, 54\ \mu_B$ are found as deep local minima whose energy is 0.133, 0.182, 0.253, 0.277 eV higher, respectively, than the lowest-energy state (Fig. 2.16).

The average bond lengths of Mn–Mn, Mn–Au, and Au–Au in the lowest-energy configuration are 2.76, 2.61, and 2.95 Å, respectively. Different spin-correlated behavior for the bond lengths of Mn–Mn, Mn–Au, and Au–Au are observed. The Mn–Mn bond lengths are more spin-sensitive at high spin states, while the Au–Au bond lengths are more spin-sensitive at the low spin states. The Mn–Au bond lengths are very sensitive to the spin states in general, and they decrease as the magnetic moments increase from 2.635 to 2.602 Å.

Mullliken population analysis on $[Mn_{13}@Au_{20}]^-$ shows that the local atomic spins on each Au atom vary from -0.24 to $0.20\ \mu_B$, and most are nearly zero, while they are around $4.0\ \mu_B$ on every Mn atom.

Most interestingly, $[Mn_{13}@Au_{20}]^-$ exhibits a giant magnetic moment ($44\ \mu_B$), whose corresponding lowest-energy state has a ferrimagnetic arrangement where one surface Mn atom is antiparallel to the rest eleven surface atoms with the local moment of -3.877 and $3.949\ \mu_B$, respectively, and the core Mn atom possesses a local moment of $2.679\ \mu_B$. For the state of $S_Z = 2\mu_B$, six surface Mn atoms are antiparallel to the rest six surface atoms with the atomic moment of 3.927 and $-4.104\ \mu_B$, respectively. The core Mn atom possesses a small moment of 3.066 μ_B. In the case of $S_z = 36\ \mu_B$, two symmetric apex Mn atoms are antiparalleled ($-3.770\ \mu_B$) to the rest eleven Mn atoms ($3.981\ \mu_B$ for the surface atoms and $2.575\ \mu_B$ for the core atom). In the case of $S_Z = 52$ and $54\ \mu_B$, all the Mn atoms are paralleled, and the local moment of Mn atoms is around $4.0\ \mu_B$. In contrast, the bare Mn_{13}^- favors a ferrimagnetic ordering with a net total moment of $2\ \mu_B$, where six surface Mn atoms have antiparallel spin arrangements ($-3.63\ \mu_B$) to the rest six surface Mn atoms ($3.85\ \mu_B$), and the core atom possesses $1.09\ \mu_B$. The ferromagnetic state of Mn_{13}^- has a total S_z of $52\ \mu_B$, while the core Mn atom possesses $0.94\ \mu_B$ and the twelve surface Mn atoms have the atomic moment of 3.72–4.59 μ_B (Fig. 2.17).

2.4 Summary

As summarized in previous sections, the core–shell magnetic clusters often exhibit new physical and chemical properties compared to their single-component counterparts. In many cases, the noble metal coating not only can enhance magnetic properties with large coercivity and high blocking temperature but also can provide sufficient resistance to the oxidation of the magnetic core. These added values in core–shell clusters pave the way for the applications of the magnetic nanoparticles in future information and biological technologies such as information storage, magnetic sensors, bioseparation, and drug delivery. Although a variety of physical and chemical techniques have been employed for their fabrication, challenges in producing uniformly coated and highly stable core–shell nanoparticles (e.g., without

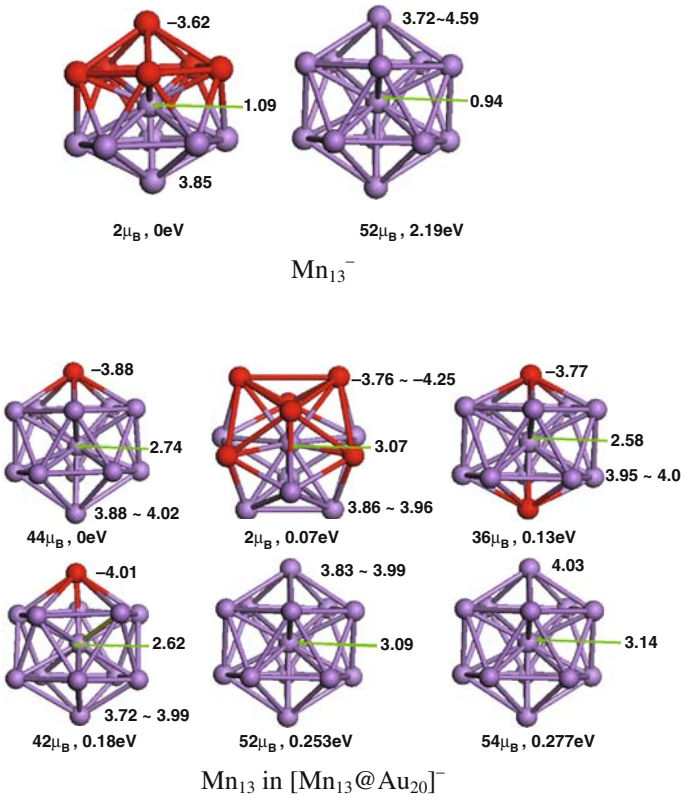

Fig. 2.17 Local spin on bare and coated Mn_{13}^- clusters in different spin states Mn_{13}^- Mn_{13} in $[Mn_{13}@Au_{20}]^-$

aggregation associated with their production) have limited wide application of the core–shell nanolclusters (or nanoparticles).

On the other hand, compared to the large amount of literature in fabrication and characterization of core–shell magnetic nanoclusters, theoretical work on the core–shell clusters is considerably less in the literature, especially on the study of nanomagnetism based on first-principles theory. Better understanding of core–shell magnetic clusters, including their structures (morphology), growth mechanics, magnetic, electronic, and optical properties are greatly needed and will definitely benefit both basic science and application. Another issue that limits extensive first-principles studies is that the core–shell nanoclusters produced in most experiments are a few to a few tens nanometers in sizes, which are beyond computational capability for the first-principles studies in most researchers' laboratory. However, the gap between the two sides is narrowing as smaller-sized core–shell clusters can be produced and characterized more routinely, and more efficient computational methodologies as well as more powerful computers are under development. We are optimistic that a

great surge in joint theoretical/experimental studies will come up in the near future, which undoubtedly will expedite our understanding and utilizing this novel form of matter.

Acknowledgement The work was supported by the National Nature Science Foundation of China (No. 10604013, 20873019), the Program for New Century Excellent Talents in the University of China (NCET-06-0470), Qinglan Project in the University of Jiangsu Province, and the Teaching and Research Foundation for the Outstanding Young Faculty of Southeast University (JW), and partly by the Office of Basic Energy Sciences (DE-FG02-04ER46164), National Science Foundation (CHE-0427746 and DMR-0820521), the Nebraska Research Initiative, and the UNL Research Computing Facility (XCZ).

References

1. Alonso, J.A.: Electronic and atomic structure, and magnetism of transition-metal clusters. Chem. Rev. **100**, 637–678 (2000).
2. Ravel, B., Carpenter, E.E., Harris, V.G.: Oxidation of iron in iron/gold core/shell nanoparticles. J. Appl. Phys. **91**, 8195–8197 (2002).
3. Baletto, F., Mottet, C., Ferrando, R.: Growth of three-shell onionlike bimetallic nanoparticles. Phys. Rev. Lett. **90**, 135504–135507 (2003).
4. Baletto, F., Mottet, C., Ferrando, R.: Growth simulations of silver shells on copper and palladium nanoclusters. Phys. Rev. B **66**, 155420–155430 (2002).
5. Baletto, F., Mottet, C., Ferrando, R.: Time evolution of Ag–Cu and Ag–Pd core–shell nanoclusters. Eur. Phys. J. D **24**, 233–236 (2003).
6. Baletto, F., Mottet, C., Rapallo, A.: Growth and energetic stability of AgNi core–shell clusters. Surf. Sci. **566–568**, 192–196 (2004).
7. Ban, Z.B., Barnakov, Y.A., Li, F., Golub, V.O., O'Connor, C.J.: The synthesis of core–shell iron@gold nanoparticles and their characterization. J. Mater. Chem. **15**, 4660–4662 (2005).
8. Bansmann, J., Baker, S.H., Binns, C., Blackman, J.A., Bucher, J.-P., orantes-Dávila, J., Dupuis, V., Favre, L., Kechrakos, D., Kleibert, A., Meiwes-Broer, K.-H., Pastor, G.M., Perez, A., Toulemonde, O., Trohidou, K.N., Tuaillon, J., Xie, Y.: Magnetic and structural properties of isolated and assembled clusters. Surf. Sci. Rep. **56**, 189–275 (2005).
9. Bao, Y., Calderon, H., Krishnan, K.M.: Synthesis and characterization of magnetic–optical Co–Au core–shell nanoparticles. J. Phys. Chem. C **111**, 1941–1944 (2007).
10. Binns, C., Trohidou, K.N., Bansmann, J., Baker1, S.H., Blackman, J.A., Bucher, J.-P., Kechrakos, D., Kleibert, A., Louch, S., Meiwes-Broer, K.-H., Pastor, G.M., Perez, A., Xie, Y.: The behaviour of nanostructured magnetic materials produced by depositing gas-phase nanoparticles. J. Phys. D: Appl. Phys. **38**, R357–R379 (2005).
11. Bloomfield, L. A., Deng, J., Zhang, H., Emmert, J.W.: in *Proc. International Symposium on Cluster and Nanostructure Interfaces*, edited by P. Jena, S. N. Khanna, and B. K. Rao, World Publishers, Singapore, 2000, p. 131.
12. Brack, M.: The physics of simple metal clusters: self-consistent jellium model and semiclassical approaches. Rev. Mod. Phys. **65**, 677–732 (1993).
13. Carpenter, E., Kumbhar, A., Wiemann, J., Srikanth, H., Wiggins, J., Zhou, W., O'Connor, C.: Synthesis and magnetic properties of gold–iron–gold nanocomposites. Mater. Sci. Eng. A **286**, 81–86 (2000).
14. Carpenter, E., Sims, J., Wienmann, J., Zhou, W., O'Conner, C.J.: Magnetic properties of iron and iron platinum alloys synthesized via microemulsion techniques. J. Appl. Phys. **87**, 5615–5617 (2000).
15. Carpenter, E.E., Sangregono, C., O′Connor, C.J.: Effects of shell thickness on blocking temperature of nanocomposites of metal particles with gold shells. IEEE Tran. Magn. **35**, 3496–3498 (1999).

16. Carpenter, E.E.: Iron nanoparticles as potential magnetic carriers. J. Magn. Magn. Mater. **225**, 17–20 (2001).
17. Caruso, F.: Nanoenginneering of particle surfaces. Adv. Mater. **13**, 11–22 (2001).
18. Chen, D., Li, J., Shi, C., Du, X., Zhao, N., Sheng, J., Liu, S.: Properties of core–shell Ni–Au nanoparticles synthesized through a redox-transmetalation method in reverse microemulsion. Chem. Mater. **19**, 3399–3405 (2007).
19. Chen, D., Wang, S.: Protective agent-free synthesis of Ni–Ag core–shell nanoparticles. Mater. Chem. Phys. **100**, 468–471 (2006).
20. Chen, M., Yamamuro, S., Farrell, D., Majetich, S.A.: Gold-coated iron nanoparticles for biomedical applications. J. Appl. Phys. **93**, 7551–7553 (2003).
21. Cho, S.J., Idrobo, J.C., Olamit, J., Liu, K., Browning, N.B., Kauzlarich, S.M., Growth mechanisms and oxidation resistance of gold-coated iron nanoparticles. Chem. Mater. **17**, 3181–3186 (2005).
22. Cho, S.J., Shahin, A.M., Long, G.J., Davies, J.E., Liu, K., Grandjean, F., Kauzlarich, S.M.: Magnetic and mössbauer spectral study of core/shell structured Fe/Au nanoparticles. Chem. Mater. **18**, 960–967 (2006).
23. Cho, S.J., Kauzlarich, S.M., Olamit, J., Liu, K., Grandjean, F., Rebbouh, L., Long, G. J.: Characterization and magnetic properties of core–shell structured Fe–Au nanoparticles. J. Appl. Phys. **95**, 6803–6806 (2004).
24. de Heer, W.A.: The physics of simple metal clusters: experimental aspects and simple models. Rev. Mod. Phys. **65**, 611–676 (1993).
25. Dorfbauer, F., Schrefl, T.: Nanostructure calculation of CoAg core–shell clusters. J. Appl. Phys. **99**, 08G706 (2006).
26. Dzhurakhalov, A., Rasulov, A., Van Hoof, T., Hou, M.: Ag–Co clusters deposition on Ag(100): an atomic scale study. Eur. Phys. J. D **31**, 53–61 (2004).
27. Dzhurakhalov, A.A., Hou, M.: Equilibrium properties of binary and ternary metallic immiscible nanoclusters. Phys. Rev. B **76**, 045429–045438 (2007).
28. Ferrando, R., Fortunelli, A., Rossi, G.: Quantum effects on the structure of pure and binary metallic nanoclusters. Phys. Rev. B **72**, 085449–085457 (2005).
29. Guevara, J., Llois, A.M., Weissmann, M.: Large variations in the magnetization of Co clusters induced by noble-metal coating. Phys. Rev. Lett. **81**, 5306–5309 (1998).
30. Guo, Z.H., Kumar, C.S.S.R., Henry, L.L., Doomes, E.E., Hormes, J., Podlaha, E.J.: Displacement synthesis of Cu shells surrounding Co nanoparticles. J. Electrochem. Soc. **152** D1–D5 (2005).
31. Haberland, H. (ed.), *Clusters of Atoms and Molecules I: Theory, experimental methods in: Cluster of atoms and molecules*. Springer-Verlag, Berlin (1994).
32. Hoof, T.V., Hou M.: Structural and thermodynamic properties of Ag–Co nanoclusters. Phys. Rev. B **72**, 115434–115445 (2005).
33. Johansson, M.P., Sundholm, D., Vaara, J.: Au_{32}: A 24-carat golden fullerene. Angew. Chem. Int. Ed. **43**, 2678–2681 (2004).
34. Jun, C.H., Park, Y.J., Yeon, Y.R., Choi, J.R., Lee, W.R., Ko, S.J., Cheon, J.: Demonstration of a magnetic and catalytic Co@Pt nanoparticle as a dual-function nanoplatform. Chem. Commun. **15**, 1619–1621 (2006).
35. Jun, Y.K., Choi, J., Cheon, J.W.: Heterostructured magnetic nanoparticles: their versatility and high performance capabilities. Chem. Commun. 1203–1214 (2007).
36. Kim, D. K., Zhang, Y., Kehr, J., Klason, T., Bjelke, B., Muhammed, M.: Characterization and MRI study of surfactant-coated superparamagnetic nanoparticles administered into the rat brain. J. Magn. Magn. Mater. **225**, 256–261 (2001).
37. Kondo, Y., Takayanagi, K.: Synthesis and characterization of helical multi-shell gold nanowires. Science. **289**, 606–608 (2000).
38. Lee, C., Chen, D.: Large-scale synthesis of Ni–Ag core–shell nanoparticles with magnetic, optical and anti-oxidation properties. Nanotechnology **17**, 3094–3099 (2006).

39. Lee, W.-R., Kim, M.G., Choi, J.-R., Park, J.-I., Ko, S.J., Oh, S.J., Cheon, J.: Redox-transmetalation process as a generalized synthetic strategy for core–shell magnetic nanoparticles. J. Am. Chem. Soc. **127**, 16090–16097 (2005).
40. Lin, J., Zhou, W.L., Kumbhar, A., Wiemann, J., Fang, J., Carpenter, E. E., O′Connor, C. J.: Gold-coated iron (Fe@Au) nanoparticles: synthesis, characterization, and magnetic field-induced self-assembly. J. Solid State Chem. **159**, 26–31(2001).
41. Liz-Marzán, L.M., Mulvaney, P.: The assembly of coated nanocrystals. J. Phys. Chem. B **107**, 7312–7326 (2003).
42. Moskovits, M.: Metal clusters. Annu. Rev. Phys. Chem. **42**, 465–499 (1991).
43. Murray, C.B., Kagan, C.R., Bawendi, M.G.: synthesis and characterization of monodisperse nanocrystals and close-packed nanocrystal assemblies. Annu. Rev. Mater. Res. **30**, 545–610 (2000).
44. Niemeyer, C.M.: Nanoparticles, proteins, and nucleic acids: biotechnology meets materials science. Angew. Chem., Int. Ed. 40, 4128–4158 (2001).
45. O'Connor, C.J., Kolesnichenko, V., Carpenter, E., Sangregorio, C., Zhou, W., Kumbhar, A., Sims, J., Agnoli, F.: Fabrication and properties of magnetic particles with nanometer dimensions. Synth. Met. **122**, 547–557 (2001).
46. Park, J.-I., Cheon, J.: Synthesis of "solid solution" and "core–shell" type cobalt–platinum magnetic nanoparticles via transmetalation reactions. J. Am. Chem. Soc. **123**, 5743–5746 (2001).
47. Park, J.-I., Kim, M. G., Jun, Y.-W., Lee, J.S., Lee, W.-R., Cheon, J.: Characterization of superparamagnetic "core–shell" nanoparticles and monitoring their anisotropic phase transition to ferromagnetic "solid solution" nanoalloys. J. Am. Chem. Soc. **126**, 9072–9078 (2004).
48. Paulus, P.M., B¨onnemann, H., van der Kraan, A.M., Luis, F., Sinzig, J., de Jongh, L.J.: Magnetic properties of nanosized transition metal colloids: the influence of noble metal coating. Eur. Phys. J. D **9**, 501–504 (1999).
49. Pyykkö, P.: Theoretical chemistry of gold. Angew. Chem. Int. Ed. **43**, 4412–4456 (2004).
50. Rivas, J., Sanchez, R.D., Fondado, A., Izco, C., Garca-Bastida, A.J., Garca-Otero, J., Mira, J., Baldomir, D., Gonzalez, A., Lado, I., Lopez- Quintela, M.A., Oserov, S.B.: Structural and magnetic characterization of Co particles coated with Ag. J. Appl. Phys. **76**, 6564–6566 (1994).
51. Rivasa, J., Garcia-Bastida, A.J., Lopez-Quintela, M.A., Ramos, C.: Magnetic properties of Co/Ag core/shell nanoparticles prepared by successive reactions in microemulsions J. Magn. Magn. Mater. **300**, 185–191 (2006).
52. Rossi, G., Rapallo, A., Mottet, C., Fortunelli, A., Baletto, F., Ferrando, R.: Magic polyicosahedral core–shell clusters. Phys. Rev. Lett. **93**, 105503–105506 (2004).
53. Sao-Joao, S., Giorgio, S., Penisson, J.M., Chapon, C., Bourgeois, S., Henry, C.: Structure and deformations of Pd–Ni core–shell nanoparticles. J. Phys. Chem. B **109**, 342–347 (2005)
54. Sobal, N.S., Ebels, U., Mohwald, H., Giersig, M.: Synthesis of core–shell PtCo nanocrystals. J. Phys. Chem. B. **107**, 7351–7354 (2003).
55. Sobal, N.S., Hilgendorff, M., Mohwald, H., Giersig, M., Spasova, M., Radetic, T., Farle, M.: Synthesis and structure of colloidal bimetallic nanocrystals: the non-alloying system Ag/Co. Nano Lett. **2**, 621–624 (2002).
56. Sun, Q., Kandalam, A. K., Wang, Q., Jena, P., Kawazoe, Y., Marquez, M.: Effect of Au coating on the magnetic and structural properties of Fe nanoclusters for use in biomedical applications: A density-functional theory study. Phys. Rev. B **73**, 134409–134414 (2006).
57. Van Hoof, T., Dzhurakhalov, A., Hou, M.: Interface formation by low energy deposition of core–shell Ag–Co nanoclusters on Ag(100). Eur. Phys. J. D **43**: 159–163 (2007).

58. Wang, J., Bai, J., Jellinek, J., Zeng, X.C.: Gold-coated transition-metal anion $[Mn_{13}@Au_{20}]$- with ultrahigh magnetic moment. J. Am. Chem. Soc. **129**, 4110–4111 (2007).
59. Wang, J., Jellinek, J., Zhao, J., Chen, Z., King, R.B., von Rague Schleyer, P.: Hollow cages versus space-filling structures for medium-sized gold clusters: the spherical aromaticity of the Au_{50} cage. J. Phys. Chem. A **109**, 9265–9269 (2005).
60. Wilcozon, J.P., Abram, B.L.: Synthesis, structure and properties of metal nanoclusters. Chem. Soc. Rev. **35**, 1162–1194 (2006).
61. Xu, Y.H., Wang, J.P.: Magnetic properties of heterostructured Co–Au nanoparticles direct-synthesized from gas phase. IEEE Tran. Magn. **43**, 3109–3111 (2007).
62. Zhang, J., Post, M., Veres, T., Jakubek, Z. J., Guan, J.W., Wang, D., Normandin, F., Deslandes, Y., Simard, B.: Laser-sssisted synthesis of superparamagnetic Fe@Au core–shell nanoparticles. J. Phys. Chem. B. **110**, 7122–7128 (2006).
63. Zhou, W., Carpenter, E., Kumbhar, A., Sims, J., O'Connor, C.: Nanophase and nanocomposite materials III. J. Mater. Res. Soc. Symp. Proc. **581**, 107–112(2000).
64. Zhou, W.L., Carpenter, E.E., Lin, J., Kumbhar, A., Sims, J., O′Connor, C.J.: Nanostructures of gold coated iron core–shell nanoparticles and the nanobands assembled under magnetic field. Eur. Phys. J. D **16**, 289–292 (2001).
65. Zhurkin, E.E., Hoof, T.V., Hou, M.: Nanoscale alloys and core–shell materials: Model predictions of the nanostructure and mechanical properties. Phys. Rev. B **75**, 224102–224116 (2007).